


Cite this: *J. Mater. Chem. A*, 2023, **11**, 1877

Non-conjugated triarylamine-based intrinsic microporous polyamides for an electrochromic supercapacitor: diffusion dynamics and charge–discharge studies†

Yu-Jen Shao,^{‡a} Tzu-Chieh Yen,^{‡a} Chien-Chieh Hu^{*b} and Guey-Sheng Liou ^{*a}

To investigate the counter ion diffusivity of polymers with intrinsic microporous structures during the electrochemical process, Tröger's base (TB) with a non-planar and V-shaped moiety was introduced to facilitate the formation of diffusion channels. The TB-incorporated polyamides (TPPA-TB and TPPA-Me-TB) revealed enhanced electrochromic properties due to higher diffusivity, which could effectively narrow down the electrochemical redox potential difference (ΔE), resulting in a higher switching response speed (ν) while maintaining similar transmittance change (ΔT). Intriguingly, the triarylamine-based polyamide TPPA-Me-TB demonstrated excellent charge–discharge ability with a high specific capacitance (C_{sp}) of 165.3 F g^{-1} at 1.0 A g^{-1} and distinct two-stage color changes from colorless to green (0.8 V) and to blue (1.2 V), which could monitor the content of charge capacity. Therefore, these novel redox-active polyamides should be attractive and suitable for electrochromic supercapacitor (ECS) materials.

Received 21st November 2022
Accepted 22nd December 2022

DOI: 10.1039/d2ta09065a

rsc.li/materials-a

Introduction

Triphenylamine (TPA)-derived polymers usually exhibit high transparency over the visible light region at the neutral state and undergo different colour changes during the redox procedure, which is suitable as electrochromic (EC) materials.^{1–3} As a promising candidate for future applications, its crucial properties, such as low oxidation voltage, short response time, and long-term stability, are indispensable, which are consistent with the eco-friendly and energy-saving characteristics. EC materials have been applied to the industry of intelligent windows (reflectance or tuneable windows) and EC displays. However, EC materials often face the dilemma of balancing EC behaviours and optical properties. Typically, a thicker film could produce a more intense visual change in the colouring state while increasing the response time and reducing the transparency simultaneously at its neutral state. Consequently, the diffusivity of counter ions within the EC films becomes a more dominant step and tremendously influences their response capability. Therefore, our group has developed several methods to promote EC behaviours, including introducing an

organic–inorganic hybrid system or porous structure into polymer films by washing out electrolyte salt. The charge-storage metal oxide nanoparticles (TiO_2 , ZrO_2) derived from an *in situ* sol–gel reaction in the polymer hybrid films provided a fast electron transfer in the redox process and could significantly enhance EC response behaviors.^{4,5} Moreover, the porous film caused by washing out the electrolyte salt could also accelerate the diffusion rate of the counter ions; however, the size of the generated pores is more prominent than two μm , which is detrimental to the transparency of the EC films at the neutral state and reduces the optical contrast ratio during the redox process in the meantime. Therefore, minimizing the pore size without sacrificing the transparency of the EC films is the main target of development. Polymers of intrinsic microporosity (PIMs) are a unique class of microporous materials reported by McKeown *et al.* and developed from phthalocyanine materials in the 1990s.⁶ In general, PIMs comprise two essential features: the presence of rigid structure units and clearly outlined concavities. Thus, the most efficient way to prepare PIMs is to introduce the stiff and contorted moieties into the polymer backbone to generate intrinsic microporosity, such as spirobifluorene (SBF),^{7–10} ethanoanthracene (EA),^{10–13} triptycene,^{14,15} and Tröger's base (TB),^{12–17} which are promising structures for preventing polymer chains from efficiently packing.^{18–20} Recently, polymers with TB scaffolds have attracted considerable attention because of their unique V-shaped conformation, forming intrinsic microporous structures applied in many fields, such as gas separation and ion-exchange membranes.^{21–29} In addition,

^aInstitute of Polymer Science and Engineering, National Taiwan University, No. 1, Sec. 4, Roosevelt Rd, Taipei 10617, Taiwan. E-mail: gsliau@ntu.edu.tw

^bGraduate Institute of Applied Science and Technology, National Taiwan University of Science and Technology, Taipei 106335, Taiwan. E-mail: cchu@mail.ntust.edu.tw

† Electronic supplementary information (ESI) available. See DOI: <https://doi.org/10.1039/d2ta09065a>

‡ The authors are equal contribution.

the non-electroactive and electroactive pentiptycene scaffolds introduced into arylamine-containing polyamides demonstrated that the V- and U- shaped cavities on the pentiptycene could facilitate the formation of intrinsic free volume to generate a large void surface in our previous reports.^{30,31} The resulting polyamides exhibit intrinsic microporosity that enhances the diffusion of counter ions of the electrolyte into the EC film during the redox process.

Recently, functionalized energy-storage electrochromic supercapacitor (ECS) materials have emerged as an attractive field owing to the visualization of storage capacity in supercapacitors. Transition metal oxides, such as tungsten trioxide (WO₃) or vanadium oxides (VO_x), are usually utilized because of their high reversibility, specific capacity, and power density.^{32–36} For instance, Im *et al.* prepared the nanofilament-embedded WO₃ ECS electrode and exhibited high specific capacitance (C_{sp}) with 214 F g⁻¹ at 0.25 mA cm⁻².³⁷ Kim *et al.* utilized WO₃ to fabricate EC film with the mesoporous structure to increase the specific area of the electrode. The resulting ECS devices performed extensive optical modulation (76% at 700 nm) with a high areal-specific capacitance of around 2.57 mF cm⁻² at 1.0 mA cm⁻².³⁸ In addition, some studies applied the electrodeposition method to prepare the conjugated polymeric film electrodes because of the high mobility of the polymer chain conformation and naturally composed mesoporous on the electrode during polymerization.^{39–45} Zhang *et al.* designed a donor-acceptor-donor monomer (CDB-EDOT) to prepare ECS electrodes by electropolymerization. The obtained polymer

exhibited 4.65 mF cm⁻² of areal-specific capacitance at 0.05 mA cm⁻² with high coloration efficiency (CE, 158 cm² C⁻¹), and the corresponding device could run a single yellow LED for more than 60 s.⁴⁵ Chao *et al.* reported a conjugated polymer with a dual-redox center (thiophene and TPA) and an electron-withdrawing cyano group by applying the electrodeposition method. The as-prepared ECS device exhibited 32.9 mF cm⁻² of capacitance (at 0.1 mA cm⁻²), high optical contrast of 67%, and outstanding cycling durability (86% capacitance and 96% optical modulation retention after 7000 cycles at 0.2 mA cm⁻²).³⁹

However, conjugated polymers prepared by electropolymerization address the critical disadvantages of intense colour at the neutral state and the limitation of processing for practical large-area applications. Consequently, in this study, we attempt to incorporate the TB scaffolds into the backbone of triarylamine-based polyamides (TPPA-TB and TPPA-Me-TB) to generate an intrinsic microporous structure in the resulting highly transparent polymer thin films cast on ITO-coated glass substrate electrodes, confirmed by wide-angle X-ray diffractometry (WXR), Brunauer-Emmett-Teller (BET) measurement, and density testing kit. Furthermore, to investigate the transport dynamics of the counter ions within the ECS thin films, the Warburg coefficient (σ_w) is utilized to calculate the diffusion coefficient (D) via electrochemical impedance spectroscopy (EIS). Interestingly, the TB-incorporated polymers demonstrate enhanced electrochemical behaviours (lower oxidation potential and narrowed redox potential difference

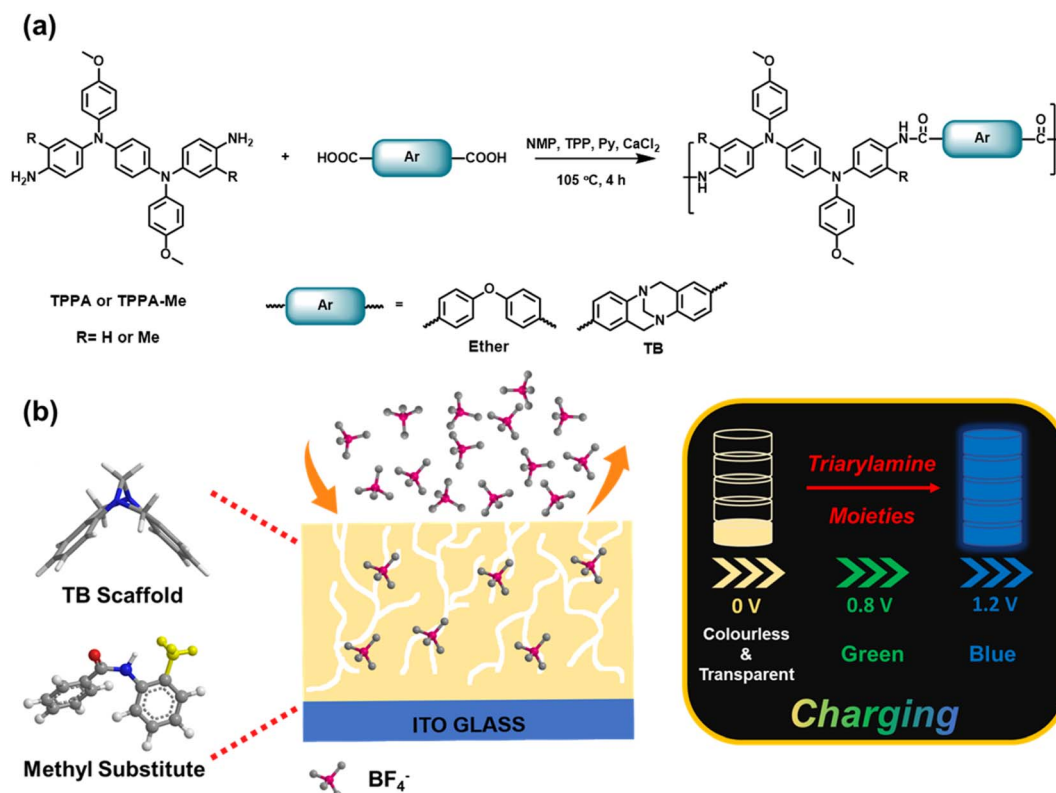


Fig. 1 (a) Structure and synthetic procedure of the polyamides studied in this work. (b) Schematic presentation of the intrinsic microporous polyamides in the study of diffusion dynamics and charge-discharge behaviours.

ΔE), higher colour efficiency (η_{CE}), and quicker response capability (t_c and t_b). In addition, apart from the conjugated polymers as the ECS materials aforementioned, the triarylamine-based polyamides, the non-conjugated polymers, are solution processable and exhibit excellent charge-discharge ability with two-stage colour change (green to blue), demonstrating that the intrinsic micropores caused by judiciously incorporating TB scaffolds and the methyl substituents (TPPA-Me-TB) could effectively enhance the C_{sp} up to 165.3 F g^{-1} at 1.0 A g^{-1} , as shown in Fig. 1. Consequently, this discovery makes triarylamine-based polyamides suitable and potential candidates for ECS materials.

Results and discussions

Characterization and basic properties of TPPA-based polyamides

The newly diamine monomer of N,N' -bis(3-methyl-4-aminophenyl)- N,N' -di(4-methoxyphenyl)- p -phenylenediamine (TPPA-Me) was prepared based on the previous report as N,N' -bis(4-aminophenyl)- N,N' -di(4-methoxyphenyl)- p -phenylenediamine (TPPA),⁴⁶ and the detailed synthetic routes are described in the ESI.† Elemental analysis, NMR, and FT-IR spectra carefully characterized all the synthesized intermediates and diamine monomers, as illustrated in Fig. S1–S12.† The corresponding polyamides could be readily prepared by direct polycondensation of the diamines, TPPA and TPPA-Me, with 4,4'-oxydibenzoic acid (ether-linkage dicarboxylic acid) and 2,8-dicarboxylic-6*H*,12*H*-5,11-methanodibenzo[*b,f*][1,5]diazocine (TB-incorporated dicarboxylic acid), respectively, as shown in Fig. 1a.^{46–48} The characterization of structures, molecular weights, and solubility tests of the resulting polymers are depicted in Fig. S13–17† and summarized in Tables S1 and S2.† All the prepared polyamides exhibited excellent solubility in common polar aprotic solvents, such as DMAc, NMP, and DMF. In addition, the thermal properties measured by applying thermogravimetric analysis (TGA) and differential scanning calorimetry (DSC) are illustrated in Fig. S18 and S19.† The prepared polymers possessed remarkable thermal stability without apparent weight loss of up to 300 °C in both air and nitrogen atmospheres. Moreover, the T_g of polymers with TB moieties increased by over 75 °C, indicating that the rigid and contorted TB units could enhance the rigidity of the polymer backbone.

Microporous properties of polyamides

The intrinsic microporosity of polyamides derived from diamines of TPPA and TPPA-Me was investigated, as depicted in Fig. 2 and tabulated in Table 1. The density of the polymers was measured with 2,2,4-trimethylpentane by employing a Mettler Toledo scale density kit. As the results displayed, the TB-incorporated polyamides showed lower density values than those of the ether-containing ones; TPPA-TB (1.171 g cm^{-3}) revealed a lower density than TPPA-Ether (1.259 g cm^{-3}), and the TPPA-Me-TB (1.144 g cm^{-3}) also exhibited a lower density in comparison to TPPA-Me-Ether (1.237 g cm^{-3}), indicating that

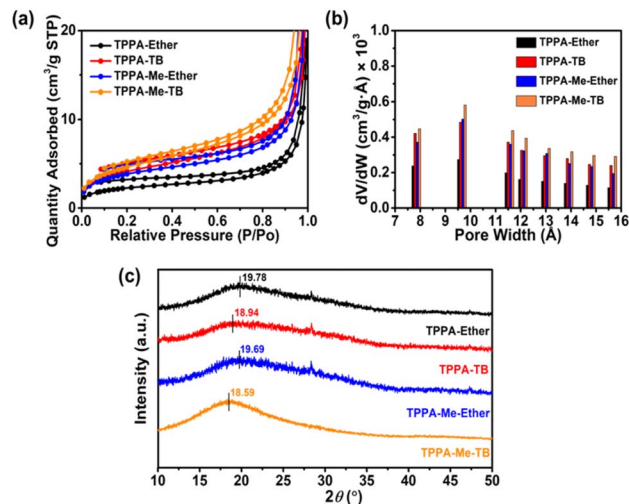


Fig. 2 (a) N_2 adsorption and desorption isotherms measured at 77 K. (b) The pore width distribution analyzed by nitrogen adsorption at 77 K via the Horvath–Kawazoe method. (c) WAXRD patterns of the polymer films (thickness: $25 \pm 5 \mu\text{m}$).

the TB scaffolds could induce more intermolecular free volume in the polymer matrix. Moreover, the methyl groups substituted in the triarylamine units could also reduce the polymer density. The specific surface areas of the TPPA- and TPPA-Me-based polymers were determined from the nitrogen adsorption/desorption isotherms at 77 K, as depicted in Fig. 2a. The results demonstrated that TPPA-TB ($14.66 \text{ m}^2 \text{ g}^{-1}$) and TPPA-Me-TB ($16.93 \text{ m}^2 \text{ g}^{-1}$) exhibited a higher surface area than the corresponding polyamides of TPPA-Ether ($7.92 \text{ m}^2 \text{ g}^{-1}$) and TPPA-Me-Ether ($13.90 \text{ m}^2 \text{ g}^{-1}$), indicating that not only could the TB scaffolds enhance the ability to form microporosity, but the methyl substituents could also effectively facilitate the ability to increase S_{BET} . Moreover, the pore size distribution was calculated by applying the Horvath–Kawazoe method based on the isotherm BET nitrogen adsorption/desorption measurement, as shown in Fig. 2b. The number of micropores between 7 Å and 16 Å pore sizes increased when the TB scaffolds and methyl substituents were introduced. It is noteworthy that the TPPA-Me-Ether with only methyl substituent could produce relative amounts of micropores to the TB-incorporated TPPA-TB, implying that both the TB scaffold and the methyl substituent possess the ability to form an intrinsic microporous

Table 1 Porosity parameters of TPPA-based polymers

Polymer	$S_{\text{BET}}^a [\text{m}^2 \text{ g}^{-1}]$	$2\theta^b [^\circ]$	d -spacing ^c [Å]	ρ [g cm^{-3}]
TPPA-Ether	7.92	19.78	4.55	1.259
TPPA-TB	14.66	18.94	4.75	1.171
TPPA-Me-Ether	13.90	19.69	4.57	1.237
TPPA-Me-TB	16.93	18.59	4.83	1.144

^a Calculated by the results of the N_2 adsorption (filled) and desorption (empty) isotherms measured by BET at 77 K. ^b Measured by XRD at the scan range of 2θ from 10° to 50° . ^c Calculated from the results of the WAXRD curve by applying Bragg's Law.

structure. Furthermore, WXR D measurement was applied, as depicted in Fig. 2c, to investigate the extent of the aggregation of the polymer chains. All polymers showed a broad diffraction peak around 19° , exhibiting certain degrees of ordered domains existing in the amorphous polymer matrix. From the WXR D data, the d -spacing values calculated as tabulated in Table 1, were 4.55 Å, 4.75 Å, 4.57 Å, and 4.83 Å for **TPPA-Ether**, **TPPA-TB**, **TPPA-Me-Ether**, and **TPPA-Me-TB**, respectively. According to the strategies for PIM materials, the TB unit has contorted and rigid V-shaped conformation, which can facilitate the generation of micropores by inefficient packing and entanglement. The methyl group in the *meta* position causes a more twisted angle of amide linkage in the *para* position, thus gaining a more significant number of micropores within the polymer film. The results also confirmed that methyl substituents and TB scaffolds in the polymer backbone could generate larger d -spacing between polymer chains owing to irregular polymer chain packing and could be beneficial in constructing more significant interchain distances within the polymer matrix in the out-of-plane direction.⁴⁹

Electrochemical properties of TPPA-based polyamide films

The polymeric electrode was prepared by drop-casting on ITO glass with further thermal treatment at 120 °C and 180 °C for 2

hours each to ensure that all the solvent was removed and made the polymer films attach to the ITO glass tightly. The electrochemical properties of drop-coated polymer films on ITO glasses were investigated by cyclic voltammetry (CV) at a scan rate of 50 mV s^{-1} in 0.1 M TBABF₄/MeCN, as shown in Fig. 3 and tabulated in Table 2. The TB-incorporated polyamides, **TPPA-TB** (0.80 V; 0.51 V) and **TPPA-Me-TB** (0.80 V; 0.47 V) exhibited lower first oxidation potential and the narrowed difference of the corresponding redox potential (ΔE) than non-TB-incorporated ones, **TPPA-Ether** (0.84 V; 0.57 V) and **TPPA-Me-Ether** (0.81 V; 0.54 V), indicating that the micropores generated by TB scaffold efficiently facilitate the diffusion ability of the counter ions to transport within the polymer film and reduce the driving potential. Moreover, the methyl group at the *ortho* position of the amide linkage revealed a narrowed ΔE value than non-methyl ones attributed to generating more micropores in the polymer films. At the second oxidation stage, the polyamides with methyl substituent behaved in a similar redox behaviour as the first stage, performing lower oxidation potential and ΔE than non-methyl ones whether introducing the TB unit or not. To clarify the influence of the methyl substituent on electrochemical behaviour, the model units, **TPPA-M** and **TPPA-Me-M** were set to apply the theoretical simulation using DFT at B3LYP/6-31G(d,p) level, as shown in Fig. S20.† **TPPA-Me-M** revealed a higher HOMO level (−4.56 eV) than **TPPA-M** (−4.62 eV) attributed to the electron-donating nature of the methyl group, resulting in the lower oxidation potential of methyl-substituted polyamides. In addition, the dihedral angle between the amide group and the attached phenyl ring in the triarylamine unit revealed a larger dihedral angle by two degrees in the presence of the methyl substituent, which is beneficial for forming an intrinsic microporous structure in the polymer film.

To investigate the transport dynamics of the counter ions within these microporous films, electrochemical impedance spectroscopy (EIS) was conducted using Randles equivalent circuit to determine the resistance of the prepared redox-active polymer films in both interfacial charge transfer and mass transfer, which comprise electrolyte resistance (R_e), charge transfer resistance (R_{ct}), and the Warburg resistance (R_w).^{50,51} As shown in Fig. 4, the diameter of semicircles in the high-frequency region represents the R_{ct} of **TPPA** and **TPPA-Me**-based polymers. According to Fig. 4a, the TB scaffolds and methyl substituents in the polymer chain could result in a lower R_{ct} for **TPPA-TB** (84 Ω), **TPPA-Me-Ether** (89 Ω), and **TPPA-Me-TB**

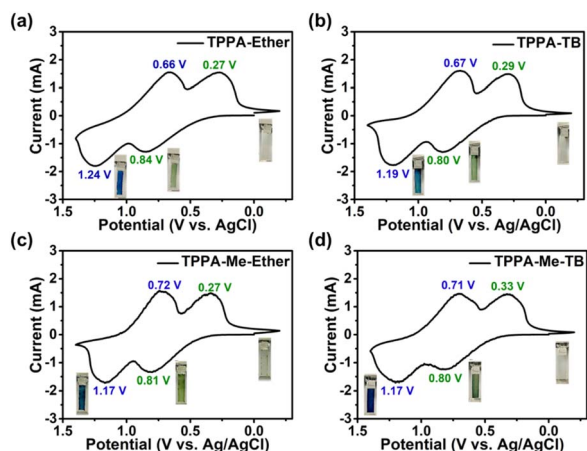


Fig. 3 Cyclic voltammetric diagrams of (a) **TPPA-Ether**, (b) **TPPA-TB**, (c) **TPPA-Me-Ether**, and (d) **TPPA-Me-TB** measured on an ITO-coated glass substrate in 0.1 M TBABF₄/MeCN at a scan rate of 50 mV s^{-1} .

Table 2 Electrochemical properties of the TPPA-based polyamides

Polymer ^a	First oxidation state			Second oxidation state		
	$E_{\text{oxi.}}^b$ [V]	$E_{\text{red.}}^c$ [V]	ΔE^d [V]	$E_{\text{oxi.}}^b$ [V]	$E_{\text{red.}}^c$ [V]	ΔE^d [V]
TPPA-Ether	0.84	0.27	0.57	1.24	0.66	0.58
TPPA-TB	0.80	0.29	0.51	1.19	0.67	0.52
TPPA-Me-Ether	0.81	0.27	0.54	1.17	0.72	0.45
TPPA-Me-TB	0.80	0.33	0.47	1.17	0.71	0.46

^a Measured relative to Ag/AgCl in MeCN (film thickness: $350 \pm 30 \text{ nm}$). ^b Oxidation potential at the peak. ^c Reduction potential at the peak. ^d Potential difference between oxidation and reduction peaks, $|E_{\text{oxi.}} - E_{\text{red.}}|$.

(82 Ω) than **TPPA-Me-Ether** (95 Ω). We speculated that the two nitrogen atoms on the TB unit could provide more hydrogen bond interaction with the ITO glasses than the ether-type diacid unit, resulting in a lower charge transfer resistance. Additionally, with the aid of the methyl group, the affinity of the electrode with the counter-ions increases and further enhances ion accessibility with reduced charge transfer resistance.⁵² Thus, **TPPA-Me-TB** would show the lowest R_{ct} value of the other polymers. Furthermore, according to the kinetic equation:

$$i = a \times v^b$$

where i is the peak current from the CV diagram and v is the scan rate (mV s^{-1}). The b value in this equation is defined from the slope value of the logarithmic plot of the scan rate and the peak current. Owing to the slope values of the resulting polyamides being around 0.8 (Fig. S21–S24†), this could be identified as the transition behaviour between the diffusion and capacitive behaviour. Therefore, considering the diffusivity of the doping ions during the redox process is essential; the diffusion coefficient was calculated by employing the Warburg coefficient (σ_w) at the low-frequency region based on the following equation:⁵⁰

$$Z' = R_e + R_{ct} + \sigma_w \omega^{-0.5}, \quad (1)$$

where ω is the angular frequency in the low-frequency region. Therefore, σ_w is determined by the slope value of Z' vs. the reciprocal root square of the ω . Furthermore, the diffusion coefficient of the doping ions (D) can be obtained from the following equation:

$$D = 0.5 \left(\frac{RT}{AF^2 \sigma_w C} \right)^2, \quad (2)$$

where R is the gas constant, T is temperature, A is the area of the electrode surface ($0.6 \times 2.5 \text{ cm}^2$), F is Faraday's constant, and C is the molar concentration of the counter ions. The results are illustrated and tabulated in Fig. 4b and Table 3, respectively. Based on the results, the TB scaffolds and methyl substituents contributed to loosely packing polymer chains and provided counter anions (BF_4^-) with a higher migration capability through the polymer matrix, resulting in a smaller σ_w . Therefore, the diffusion coefficient (D) was two times g either in the **TPPA** or **TPPA-Me** with TB scaffolds, implying that the counter ions are transported more efficiently with less resistance. The results indicated that the parameters of ion diffusing generally behaved in accordance with the tendency of microporous characteristics. After 1000 cycles of CV scanning of **TPPA-Me-TB**, the R_{ct} value slightly increases by 9% ($\approx 7 \Omega$), with a similar slope in the mass-control region (low-frequency region), indicating that the microporous conformation from this rigid polymer for the diffusivity of the counter-ions can be retained after a thousand cycles, as depicted in Fig. S25.†

Electrochromic properties of polyamide films

The electrochromic properties of polyamide films with a similar thickness (*ca.* 350 nm) were determined by spectroelectrochemical measurements. All the polymer films cast on the ITO glass exhibited high transparency in the visible region, as illustrated in Fig. 5 and Fig. S26–S29.† All the prepared polymer films revealed a greenish appearance with increasing

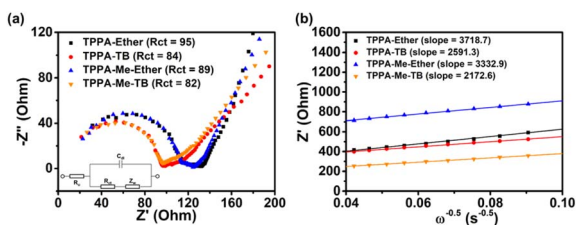


Fig. 4 (a) Nyquist plots and (b) the relationship curves between Z' and $\omega^{-0.5}$ at the low frequencies of the prepared polymer films under oxidation state.

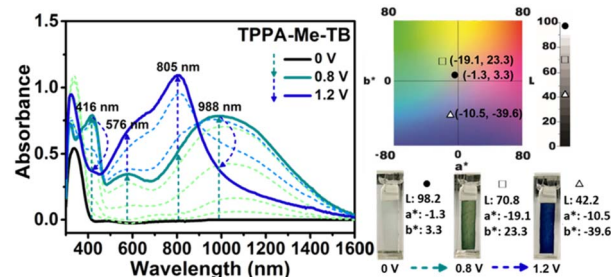


Fig. 5 Spectroelectrochemical spectra of **TPPA-Me-TB** measured on an ITO-coated glass substrate in 0.1 M $\text{TBABF}_4/\text{MeCN}$ (thickness: 350 \pm 30 nm).

Table 3 Electrochemical impedance and electrochromism of TPPA-based polyamides

Polymer	R_{ct} ^a [Ω]	σ_w ^b [$\Omega \text{ cm}^2 \text{ s}^{-0.5}$]	D ^c [$\text{cm}^2 \text{ s}^{-1} 10^{-19}$]	ΔT ^d [%]	η_{CE} ^e [$\text{cm}^2 \text{ C}^{-1}$]	v^f [% s^{-1}]
TPPA-Ether	95	3718.7	0.8	77.6	207	8.62
TPPA-TB	84	2591.3	1.6	81.4	280	9.40
TPPA-Me-Ether	89	3332.9	1.0	77.7	307	15.20
TPPA-Me-TB	82	2172.6	2.3	78.4	345	16.04

^a The resistance of charge transfer. (thickness: 350 \pm 30 nm). ^b Warburg coefficient slope for the plot of Z' vs. the reciprocal root square of the lower angular frequency. ^c Diffusion coefficient of the doping ions. ^d Optical contrast ratio is $\Delta T = T_b - T_c$, where T_b and T_c are the transmittances of bleaching and colouring states, respectively. ^e Coloration efficiency is defined as the slope of the δOD vs. Q . ^f Response speed is defined as 90% of ΔT divided by t_c .

absorption at around 420 nm, 580 nm, and 1000 nm at the first oxidation stage. The absorption in the NIR region could be attributed to the intervalence charge transfer (IV-CT) from the strong electron coupling of the **TPPA** cation radical.⁵³ Upon the secondary oxidation process, the absorption intensities at around 580 nm and 820 nm increased, while the characteristic absorption of IV-CT around 1000 nm disappeared, changing the film to blue. The response capability and electrochemical stability of the EC polymer films in the first oxidation state were conducted by applying a square wave potential step method between 0.8 V (ON) and -0.2 V (OFF) equipped with optical spectroscopy in TBABF₄/MeCN solution to evaluate the switching response time and stability. The response time is defined as the time of EC materials for absorbance at a specific wavelength (433 nm), reaching 90% of the saturated absorption change during the redox-switching process. According to Fig. 6 and Table S3,[†] the prepared polyamides with TB moiety exhibited a shorter response time than those without TB moiety either in the colouring and bleaching time, t_c and t_b , respectively. In addition, the polyamides with methyl substituents revealed a shorter response time than those without the methyl group. Consequently, the **TPPA-Me-TB** merging TB scaffold and the methyl substituents demonstrate the synergetic effect, resulting in the fastest response performance with the colouring and bleaching time, t_c and t_b , of 4.4 s (45.7% lower) and 2.2 s (48.8% lower) when compared with **TPPA-Ether**, respectively. In addition, among the ejecting charges integrated by the monitoring diagram of the i - t technique, either the TB or methyl-incorporated polyamides, **TPPA-TB** (η_{CE} : 310 cm² C⁻¹; ν : 9.40% s⁻¹), **TPPA-Me-Ether** (η_{CE} : 269 cm² C⁻¹; ν : 15.20% s⁻¹), and **TPPA-Me-TB** (η_{CE} : 345 cm² C⁻¹; ν : 16.04% s⁻¹), revealed a sharper and lower amount of ejecting charge during the oxidation or reduction process and gained a higher η_{CE} and response speed (Fig. S30–S31[†] and Table 3) than the structurally related polyamide of **TPPA-Ether** (η_{CE} : 207 cm² C⁻¹; ν : 8.62% s⁻¹). Moreover, all the prepared polyamide films exhibited

excellent stability with the reversibility of transmittance contrast above 86% after 500 cycles, as shown in Fig. S32.[†]

Capacitive properties of polyamide films

The galvanostatic charge–discharge (GCD) technique was used to evaluate the charge–discharge behaviours of the redox-active non-conjugated triarylamine-based polymers. According to Fig. S21–S24,[†] the prepared polyamide films revealed a hybrid behaviour of diffusion and capacitive control characteristics. Herein, the GCD curves at different current densities (0.5–10 A g⁻¹) were illustrated with capacitive properties between 1.2 V and 0 V (Fig. S33 and S34[†]). Unlike the conventional pseudocapacitor, this material is probably a battery-type (hybrid-type) pseudocapacitor. Based on the references, the first sharp peak drop from the discharge profile is mainly attributed to the material's double-layer capacitive discharge, followed by the phase transformation plateau with an extended discharge time for reactant diffusion into the inner pores for the battery-type reaction, and the final drop can be attributed to the concentration polarization of the material.^{54–56}

In Fig. S33a,[†] **TPPA-Ether** exhibited a symmetric charge–discharge characteristic pattern with a specific capacitance (C_{sp}) of 111.8 F g⁻¹ at 1.0 A g⁻¹ and a coulombic efficiency of 93.5% and could remain high C_{sp} of 97.5 F g⁻¹ even in the case of high current density (10 A g⁻¹). Furthermore, by incorporating the TB scaffold in the polymer chain of **TPPA-TB**, the C_{sp} could increase to 117.5 F g⁻¹ at 1.0 A g⁻¹, implying that the higher specific surface area facilitates the counter ions efficiently transporting within the polymer film to enhance the capacitive performance, comprising the R_{ct} and diffusion coefficient values measured by EIS.⁵⁷ Similarly, as tabulated in Table 4, **TPPA-Me-Ether** and **TPPA-Me-TB** also exhibited a similar trend: **TPPA-Me-TB** merging TB scaffold and the methyl substituents demonstrate the synergetic effect, resulting in higher C_{sp} (165.3 F g⁻¹ at 1.0 A g⁻¹) than **TPPA-Me-Ether** without TB moiety (158.9 F g⁻¹ at 1.0 A g⁻¹). Interestingly, the methyl-incorporated polyamides revealed a 40% C_{sp} enhancement compared with the non-methyl ones. The reason for C_{sp} enhancement could be attributed to the presence of the electron-donating methyl groups in the phenyl ring to gain a higher tendency of the counter ions onto the polymer chain.^{58,59} Intriguingly, the C_{sp} values of the resulting polyamide films could be maintained at around 100 F g⁻¹ even at a high current density process; for example, **TPPA-Me-TB** exhibited 100.8 F g⁻¹ at 10 A g⁻¹. The areal-specific capacitance (C_{areal}) of these polyamides could be converted by the active area of the electrode (2.5 cm × 2.5 cm) and the mass-dependent GCD results for comparison. The calculated C_{areal} values confirmed superior performance with 14.23, 14.95, 20.21, and 21.02 mF cm⁻² for **TPPA-Ether**, **TPPA-TB**, **TPPA-Me-Ether**, and **TPPA-Me-TB**, respectively.

Furthermore, the prepared polyamides manifested distinct two-stage colour changes that could evaluate and monitor the energy storage from 0.0 V (colourless) to the first charge state, 0.8 V (green), or the second charge state, 1.2 V (blue), with significant transmittance responses at 416 nm, 576 nm, and 805 nm, as shown in Fig. 7b and ESI[†] Video. In addition, these

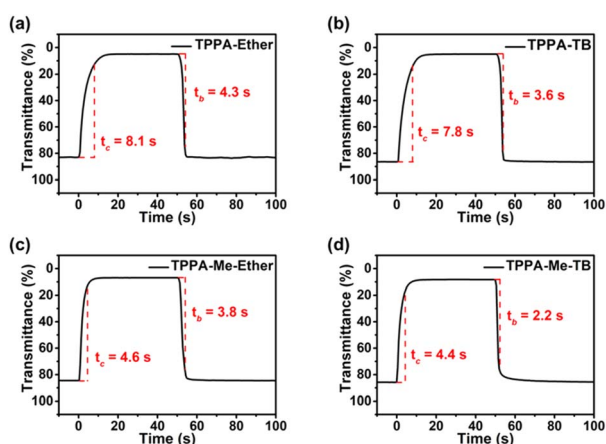


Fig. 6 Switching response time of (a) **TPPA-Ether**, (b) **TPPA-TB**, (c) **TPPA-Me-Ether**, and (d) **TPPA-Me-TB** films on the ITO-coated glass substrate (coated area: 0.6 cm × 3 cm; thickness: 350 ± 30 nm) at 433 nm in 0.1 M TBABF₄/MeCN with 0.8 V as colouring voltage and -0.2 V as bleaching voltage.

Table 4 Performance comparison of the polymeric electrode ECS materials

Materials	Electrolyte	C_{sp} or C_{areal}	Ref.
PETC	LiClO ₄ /PC	82.2 F g ⁻¹ (41.1 mF cm ⁻²) @ 0.01 mA cm ⁻²	39
pCDB-EDOT	TBAPF ₆ /MeCN	4.65 mF cm ⁻² @ 0.05 mA cm ⁻²	45
6FDA-HBPI	TBAP/MeCN	69 F g ⁻¹ @ 0.5 A g ⁻¹	57
PCBDTP	LiClO ₄ /PC	42 F g ⁻¹ (2.5 mF cm ⁻²) @ 0.1 mA cm ⁻²	60
MWCNT-PBDTC	LiClO ₄ /PC	175 F g ⁻¹ (17.5 mF cm ⁻²) @ 0.5 mA cm ⁻²	61
poly(BT-Th-EDOT)	TBAPF ₆ /MeCN	92 F g ⁻¹ @ 1.0 A g ⁻¹	62
poly(EDOT-BE-O)	TBAPF ₄ /MeCN	97 F g ⁻¹ @ 1.0 A g ⁻¹	63
P1	LiClO ₄ /PC	21.59 mF cm ⁻² @ 0.075 mA cm ⁻²	64
PI-IDT	TBAPF ₄ /PC	6.2 mF cm ⁻² @ 0.05 mA cm ⁻²	68
TPPA-Ether	TBAPF ₄ /MeCN	111.8 F g ⁻¹ (14.23 mF cm ⁻²) @ 1 A g ⁻¹	This work
TPPA-TB	TBAPF ₄ /MeCN	117.5 F g ⁻¹ (14.95 mF cm ⁻²) @ 1 A g ⁻¹	This work
TPPA-Me-Ether	TBAPF ₄ /MeCN	159.8 F g ⁻¹ (20.21 mF cm ⁻²) @ 1 A g ⁻¹	This work
TPPA-Me-TB	TBAPF ₄ /MeCN	165.3 F g ⁻¹ (21.02 mF cm ⁻²) @ 1 A g ⁻¹	This work

polyamides exhibited superior performances in some aspects of the ΔT and C_{sp} or C_{areal} to the recent research on the single polymeric electrode, as illustrated in Fig. 7c and 7d and Table 4. It is commendable that only very few reports could produce charge–discharge ability with both moderate C_{sp} and electrochromic optical contrast for the non-conjugated polymeric materials.^{57,68} For example, the thiophene-based polyimide, PI-IDT, performed only 6.2 mF cm⁻² at 0.05 mA cm⁻² with low optical transmittance contrast of 21.8%. In addition, the resulting intrinsic microporous triarylamine-based polyamides exhibited properties comparable to those of mesoporous conjugated polymer films prepared using the electrodeposition method. The polymeric electrodes derived by applying the electrodeposition method usually exhibits high C_{areal} in per unit area but reveal only low C_{sp} when converting from per unit area to per unit mass. Simultaneously, these non-conjugated polyamides in this study could demonstrate more accurate capacitance by controlling the amount of material used in the casting

process. Consequently, solution-processable triarylamine-based polyamides with bulky and twisted structures for developing intrinsic microporosity can be a more feasible and judicious way to produce large-scale ECS materials.

Conclusions

In this study, a series of triarylamine-based polyamides was designed and prepared to investigate the effect of introducing the TB scaffold and methyl substituents on the performance of electrochemical behaviors. The specific surface area, d -spacing, and density results demonstrate that incorporating TB or methyl group into polyamides could generate more intrinsic micropores in the prepared films. The resulting intrinsic micropores effectively enhanced the diffusion dynamics of the counter ions within the redox-active polymer films and significantly improved the electrochromic characteristics, such as the lower oxidation potential, shorter response capability, and higher η_{CE} . It is noteworthy that the **TPPA-Me-TB** merging TB scaffold and the methyl substituents demonstrate the synergistic effect, resulting in the reduction of the coloring and bleaching time, t_c and t_b , by 4.4 s (45.7% lower) and 2.2 s (48.8% lower) when compared with **TPPA-Ether**, respectively. In addition, this new series of polymers, triarylamine-based polyamides, revealed an intriguing discovery suitable for applying ESC materials, ascribed to the intrinsic micropores and higher specific surface area in the prepared films caused by the synergistic effect from the TB scaffold, and the methyl substituents enhanced C_{sp} by at least 40%. Furthermore, these redox-active polyamides exhibited two-stage distinct color changes from low voltage (0.8 V, green) to high voltage (1.2 V, blue), which are consequently helpful in monitoring the storage energy of the fabricated supercapacitors.

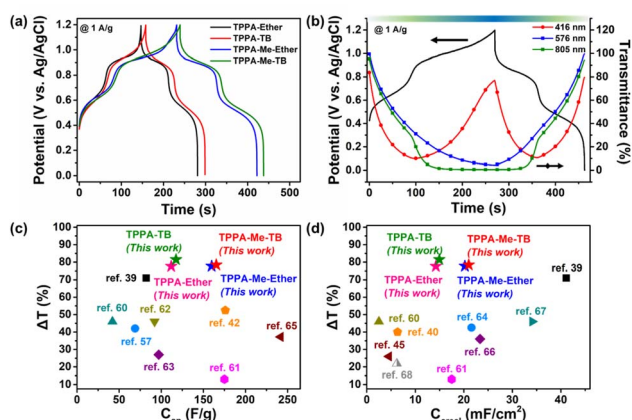


Fig. 7 (a) Galvanostatic charge–discharge curves of prepared polyamide films in a three-electrode configuration at different current densities in 0.1 M TBAPF₄/MeCN. (b) GCD curve at a current density of 1 A g⁻¹ (black line) and the transmittance changes at 416 nm, 576 nm, and 805 nm (red, blue, and green lines, respectively) in the case of TPPA-Me-TB (thickness: 375 ± 30 nm). (c) and (d) Plots of ΔT vs. C_{sp} and C_{sp} vs. C_{areal} , respectively, compared to the references.^{39,42,45,60–68}

Author contributions

Y.-J. Shao measured the electrochemical properties and prepared the draft of the manuscript. Y.-C. Yen synthesized the monomers and polymers, measured the basic properties of the resulting polymers, and prepared the draft of the manuscript.

C.-C. Hu provided the instrument for the microporous measurement and revised the manuscript. G.-S. Liou designed the concept and the chemical structures, guided and supervised the project, and revised the manuscript.

Conflicts of interest

There are no conflicts to declare.

Acknowledgements

This work was financially supported by the Ministry of Science and Technology in Taiwan (MOST 111-2113-M-002-024, and 111-2221-E-002-028-MY3). The authors acknowledge MOST for research support (MOST 111-2731-M-002-001, EA0002).

Notes and references

- C. W. Chang, G. S. Liou and S. H. Hsiao, *J. Mater. Chem.*, 2007, **17**, 1007–1015.
- H. J. Yen, H. Y. Lin and G. S. Liou, *Chem. Mater.*, 2011, **23**, 1874–1882.
- H. J. Yen and G. S. Liou, *Chem. Mater.*, 2009, **21**, 4062–4070.
- B. C. Pan, W. H. Chen, T. M. Lee and G. S. Liou, *J. Mater. Chem. C*, 2018, **6**, 12422–12428.
- Y. W. Chiu, M. H. Pai and G. S. Liou, *ACS Appl. Mater. Interfaces*, 2020, **12**, 35273–35281.
- N. B. McKeown, *Phthalocyanine materials: synthesis, structure and function*, Cambridge University Press, 1998.
- C. G. Bezzu, M. Carta, A. Tonkins, J. C. Jansen, P. Bernardo, F. Bazzarelli and N. B. McKeown, *Adv. Mater.*, 2012, **24**, 5930–5933.
- X. Ma, O. Salinas, E. Litwiller and I. Pinnau, *Macromolecules*, 2013, **46**, 9618–9624.
- R. Seto, Y. Koyama, K. Xu, S. Kawauchi and T. Takata, *Chem. Commun.*, 2013, **49**, 5486–5488.
- C. G. Bezzu, M. Carta, J. C. Ferrari, M. Jansen, E. Monteleone, E. Esposito, A. Fuoco, K. Hart, T. Liyana-Arachchi and C. M. Colina, *J. Mater. Chem. A*, 2018, **6**, 10507–10514.
- T. Emmler, K. Heinrich, D. Fritsch, P. M. Budd, N. Chaukura, D. Ehlers, K. Rätzke and F. Faupel, *Macromolecules*, 2010, **43**, 6075–6084.
- M. Carta, R. Malpass-Evans, M. Croad, Y. Rogan, J. C. Jansen, P. Bernardo, F. Bazzarelli and N. B. McKeown, *Science*, 2013, **339**, 303–307.
- E. Tocci, L. De Lorenzo, P. Bernardo, G. Clarizia, F. Bazzarelli, N. B. McKeown, M. Carta, R. Malpass-Evans, K. Friess and K. T. Pilnáček, *Macromolecules*, 2014, **47**, 7900–7916.
- B. S. Ghanem, *Polym. Chem.*, 2012, **3**, 96–98.
- B. S. Ghanem, R. Swaidan, E. Litwiller and I. Pinnau, *Adv. Mater.*, 2014, **26**, 3688–3692.
- M. Carta, R. Malpass-Evans, M. Croad, Y. Rogan, M. Lee, I. Rose and N. B. McKeown, *Polym. Chem.*, 2014, **5**, 5267–5272.
- M. Carta, M. Croad, J. C. Jansen, P. Bernardo, G. Clarizia and N. B. McKeown, *Polym. Chem.*, 2014, **5**, 5255–5261.
- H. Mark, *Encyclopedia of Space Science & Technology*, Wiley-Interscience, 2003.
- O. Ilinitich, V. Fenelonov, A. Lapkin, L. Okkel, V. Terskikh and K. Zamaraev, *Microporous Mesoporous Mater.*, 1999, **31**, 97–110.
- N. B. McKeown, S. Makhseed and P. M. Budd, *Chem. Commun.*, 2002, **23**, 2780–2781.
- O. V. Rúnarsson, J. Artacho and K. Wärnmark, *Eur. J. Org. Chem.*, 2012, **2012**, 7015–7041.
- M. Carta, R. Malpass-Evans, M. Croad, Y. Rogan, J. C. Jansen, P. Bernardo and N. B. McKeown, *Science*, 2013, **339**, 303–307.
- Y. Zhuang, J. G. Seong, Y. S. Do, W. H. Lee, M. J. Lee, M. D. Guiver and Y. M. Lee, *J. Membr. Sci.*, 2016, **504**, 55–65.
- Z. Wang, D. Wang, F. Zhang and J. Jin, *ACS Macro Lett.*, 2014, **3**, 597–601.
- Y. Xiao, L. Zhang, L. Xu and T. S. Chung, *J. Membr. Sci.*, 2017, **521**, 65–72.
- M. Lee, C. G. Bezzu, M. Carta, P. Bernardo, G. Clarizia, J. C. Jansen and N. B. McKeown, *Macromolecules*, 2016, **49**, 4147–4154.
- Z. Yang, R. Guo, R. Malpass-Evans, M. Carta, N. B. McKeown, M. D. Guiver and T. Xu, *Angew. Chem., Int. Ed.*, 2016, **128**, 11671–11674.
- J. Zhou, Z. Jiao, Q. Zhu, Y. Li, L. Ge, L. Wu and T. Xu, *J. Membr. Sci.*, 2021, **627**, 119246.
- J. Zhou, Y. Liu, P. Zuo, Y. Li, Y. Dong, L. Wu and T. Xu, *J. Membr. Sci.*, 2021, **620**, 118832.
- Y. W. Chiu, W. S. Tan, J. S. Yang, M. H. Pai and G. S. Liou, *Macromol. Rapid Commun.*, 2020, **41**, 2000186.
- M. H. Pai, C. C. Hu, W. S. Tan, J. S. Yang and G. S. Liou, *ACS Macro Lett.*, 2021, **10**, 1210–1215.
- S. Wang, H. Xu, J. Zhao and Y. Li, *Inorg. Chem. Front.*, 2022, **9**, 514–523.
- W. Li, J. Zhang, Y. Zheng and Y. Cui, *Sol. Energy Mater. Sol. Cells*, 2022, **235**, 111488.
- P. Wang, Y. Sun, J. Li, G. Zhu, X. Zhang, H. Yang and B. Lin, *J. Alloys Compd.*, 2022, **922**, 166195.
- A. K. Prasad, J. Y. Park, S. H. Kang and K. S. Ahn, *Electrochim. Acta*, 2022, **422**, 140340.
- D. Mohanadas, N. H. N. Azman and Y. Sulaiman, *J. Energy Storage*, 2022, **48**, 103954.
- J. Kim, A. I. Inamdar, Y. Jo, S. Cho, A. T. A. Ahmed, B. Hou and H. Im, *J. Mater. Chem. A*, 2022, **8**, 13459–13469.
- K. W. Kim, T. Y. Yun, S. H. You, X. Tang, J. Lee, Y. Seo and J. K. Kim, *NPG Asia Mater.*, 2020, **12**, 1–10.
- Y. Zhang, F. Q. Bai, Y. Xie, M. Zhu, L. Zhao, D. An and D. Chao, *Chem. Eng. J.*, 2022, **450**, 138386.
- Y. Tang, L. Zhang, S. Yan, Y. Kuai, H. Fu, W. Li and C. Zhang, *Sol. Energy Mater. Sol. Cells*, 2022, **245**, 111857.
- X. Lv, J. Li, L. Zhang, M. Ouyang, A. Tameev, A. Nekrasov and C. Zhang, *Chem. Eng. J.*, 2022, **431**, 133733.
- W. Yao, P. Liu, C. Liu, J. Xu, K. Lin, H. Kang and F. Jiang, *Chem. Eng. J.*, 2022, **428**, 131125.
- R. Wang, J. Li, L. Gao and J. Yu, *Chem. Eng. J.*, 2022, **445**, 136731.
- S. Topal, O. S. Ipek, E. Sezer and T. Ozturk, *Chem. Eng. J.*, 2022, **434**, 133868.

- 45 Q. Huang, J. Chen, S. Yan, X. Shao, Y. Dong, J. Liu and C. Zhang, *ACS Sustainable Chem. Eng.*, 2021, **9**, 13807–13817.
- 46 H. J. Yen and G. S. Liou, *Chem. Mater.*, 2009, **21**, 4062–4070.
- 47 Z. Zhu, J. Zhu, J. Li and X. Ma, *Macromolecules*, 2020, **53**, 1573–1584.
- 48 A. F. El-Mahdy, J. Lüder, M. G. Kotp and S. W. Kuo, *Polymers*, 2021, **13**, 1385.
- 49 Y. Zhuang, J. G. Seong, Y. S. Do, H. J. Jo, Z. Cui, J. Lee, Y. M. Lee and M. D. Guiver, *Macromolecules*, 2014, **47**, 3254–3262.
- 50 X. Lv, S. Yan, Y. Dai, M. Ouyang, Y. Yang, P. Yu and C. Zhang, *Electrochim. Acta*, 2015, **186**, 85–94.
- 51 Y. Xia, W. Zhang, H. Huang, Y. Gan, Z. Xiao, L. Qian and X. Tao, *J. Mater. Chem.*, 2011, **21**, 6498–6501.
- 52 Y. Lu, J. Liang, S. Deng, Q. He, S. Deng, Y. Hu and D. Wang, *Nano Energy*, 2019, **65**, 103993.
- 53 H. J. Yen, S. M. Guo, G. S. Liou, J. C. Chung, Y. C. Liu, Y. F. Lu and Y. Z. Zeng, *J. Polym. Sci., Part A: Polym. Chem.*, 2011, **49**, 3805–3816.
- 54 Y. Jiang and J. Liu, *Energy Environ. Mater.*, 2019, **2**, 30–37.
- 55 J. Xie, P. Yang, Y. Wang, T. Qi, Y. Lei and C. M. Li, *J. Power Sources*, 2018, **401**, 213–223.
- 56 B. Wang, L. Wang, H. Chen, Y. Jia and Y. Ma, *Adv. Opt. Mater.*, 2022, 2201572.
- 57 N. Sun, S. Meng, Z. Zhou, D. Chao, Y. Yu, K. Su and C. Chen, *Electrochim. Acta*, 2017, **256**, 119–128.
- 58 C. Sivakumar, J. N. Nian and H. Teng, *J. Power Sources*, 2005, **144**, 295–301.
- 59 M. Li, R. Ramachandran, Y. Wang, Q. Chen and Z. X. Xu, *Chin. J. Chem.*, 2021, **39**, 1265–1272.
- 60 Y. Sun, G. Zhu, X. Zhao, W. Kang, M. Li, X. Zhang, H. Yang, L. Guo and B. Lin, *Sol. Energy Mater. Sol. Cells*, 2020, **215**, 110661.
- 61 T. Ye, Y. Sun, X. Zhao, B. Lin, H. Yang, X. Zhang and L. Guo, *J. Mater. Chem. A*, 2018, **6**, 18994–19003.
- 62 S. Ming, Z. Li, S. Zhen, P. Liu, F. Jiang, G. Nie and J. Xu, *Chem. Eng. J.*, 2020, **390**, 124572.
- 63 S. Ming, K. Lin, H. Zhang, F. Jiang, P. Liu, J. Xu, G. Nie and X. Duan, *Chem. Commun.*, 2020, **56**, 5275–5278.
- 64 P. Wang, Y. Sun, J. Li, G. Zhu, X. Zhang, H. Yang and B. Lin, *Chem. Eng. J.*, 2022, **446**, 137330.
- 65 Y. Zhang, E. B. Berda, X. Jia, Z. Lu, M. Zhu and D. Chao, *ACS Appl. Polym. Mater.*, 2020, **2**, 3024–3033.
- 66 Q. Guo, J. Li, B. Zhang, G. Nie and D. Wang, *ACS Appl. Mater. Interfaces*, 2019, **11**, 6491–6501.
- 67 Q. Guo, X. Zhao, Z. Li, D. Wang and G. Nie, *Chem. Eng. J.*, 2020, **384**, 123370.
- 68 Y. Sun, X. Zhao, G. Zhu, M. Li, X. Zhang, H. Yang and B. Lin, *Electrochim. Acta*, 2020, **333**, 135495.